Resonant Spectra of Malignant Breast Cancer Tumors Using the Three-Dimensional Electromagnetic Fast Multipole Model

Magda El-Shenawee, *Senior Member, IEEE*

***Abstract*—This paper presents an intensive numerical study of the resonance scattering of malignant breast cancer tumors. The three-dimensional electromagnetic model, based on the equivalence theorem, is used to obtain induced electric and magnetic currents on breast and tumor surfaces. The results show that the nonspherical malignant tumor can be characterized, based on its spectra, regardless of orientation, incident polarization, or incident or scattered directions. The spectra of the tumor depend solely upon its physical characteristics (i.e., shape and electrical properties); however, their locations are not functions of the depth of the tumor beneath the breast surface. This paper can be a guide in the selection of the frequency range at which the tumor resonates to produce the maximum signature at the receiver.**

***Index Terms*—Breast cancer, computational electromagnetics, resonance, steepest descent fast multipole method.**

I. Introduction

MEDICAL science has conducted extensive research in recent years in an effort to detect and cure breast cancer; however, this disease still remains potentially life threatening for many women. Researchers have developed and used several imaging modalities to detect breast cancer. Among them are mammography, which is currently considered to be the most reliable method; ultrasound; and magnetic resonance imaging, as reported in [1], [2]. In addition, medical applications have used microwave imaging [3]. The electrical properties of normal breast tissues, benign and/or malignant tumors, and the breast skin layer are key issues for this modality. Research reports the measurements of the electric dielectric constants of these tissues over a certain range of frequencies [4]–[11]. Recently, microwave tomography has shown promises in the early detection of breast cancer [12], [13]. In addition, microwave radar technology has been investigated to detect and image malignant breast tumors [14]–[24]. Clinical prototypes for microwave imaging of the breast are presented in [14]–[17]. The papers [18]–[24] cite the computational electromagnetic method, the finite-difference time-domain, along with signal processing techniques to simulate and analyze several microwave systems.

Manuscript received July 11, 2002; revised May 11, 2003. This work was supported in part by the NASA Langley Research Center under Grant US/NASA/NAG-1-020 and in part by Northeastern University through National Science Foundation (NSF)-ERC Award EEC-9 986 821.

The author is with the Department of Electrical Engineering, University of Arkansas, 3217 Bell Engineering Center, Dicksen Street, Fayetteville, AR 72701 USA (e-mail: magda@uark.edu).

Digital Object Identifier 10.1109/TBME.2003.820392

In previous research on the humanitarian anti-personnel mine detection application using ground penetrating radar (GPR), it proved to be very difficult to distinguish between the scattered signal from rough ground where a small plastic mine was buried and the scattered signal from rough ground without buried mines [25]–[28]. This difficulty was due to the small size of the mine relative to the wavelength. In some cases, the soil medium was very lossy, and in other cases the electrical properties of the mine were very similar to those of the surrounding dry soil. In addition, the considerable clutter due to the presence of random rough ground, inhomogeneous soil, and the presence of benign objects nearby the target significantly obscured the detection process.

Similarly, in the breast cancer application, several comparable difficulties occur: normal breast tissue is lossy at microwave frequencies, tumors are very small in cases of early detection, and the breast tissue is heterogeneous. These factors make detecting a tumor in the breast as difficult as sensing the plastic target in the minefield.

The purpose of this paper is to investigate and analyze the behavior of the signature of the tumor over the frequency range 1–10 GHz with the intent to determine the frequencies at which the signature reaches its maximum. Several researchers have reported that dielectric and conducting objects can resonate at certain frequencies in the electromagnetic spectrum [29]–[40]. When these frequencies are independent of excitation, they are located in the complex plane and are known as the *natural frequencies*. Their locations depend only on the size, shape, and material of the object. On the other hand, these objects can also resonate upon excitation with a continuous wave at real frequencies, as reported in [29], where Mie solution was used. The resonating objects were located in free space in [29]–[37], while they were imbedded under an interface in [38]–[40]. In [29], the plane waves excited the immersed object in free space, and the scattered radiation was monitored as a function of frequency, in order to obtain their resonance spectrum. This approach is used here to determine the resonance spectra of malignant tumors located inside normal breast tissue, as cited in [18]. Since the dielectric constants of malignant tumors are very lossy, they act as low Q-resonators. Moreover, the magnitude of the scattered waves at resonant frequencies is considerably reduced due to the absorption of transmitted waves by breast tissue. These scattered fields exhibit an obvious resonant radiation when a tumor is present inside the breast. It is important to emphasize that the current work focuses on lossy objects under an interface, i.e., inhomogeneous lossy medium, while the work pre-

sented in [29] focused on lossless dielectric objects immersed in free space. While the Mie solution was used in [29], this paper utilizes a frequency-domain fast computational electromagnetic technique. This technique is based on the fast multipole method hybridized with the steepest descent integration rule (SDFMM) [41]–[44] and [25]–[28]. In particular, this paper utilizes the multiple interaction model (MIM) combined with the SDFMM (MIM-SDFMM [45]) to compute the intensity scattered from the breast. The MIM-SDFMM is validated by the method of moments (MoM), as demonstrated in Section III.

Section II discusses the formulations of the electromagnetic model, Section III discusses the numerical results, and Section IV summarizes the concluding remarks.

II. Methods

This research utilized the three-dimensional (3-D) rigorous electromagnetic model, based on the classical equivalence theorem, to simulate the scattering from malignant tumors located in normal breast tissue. This model was successfully implemented in humanitarian anti-personnel plastic mine detection [25]–[28]. In this model, the surfaces of the breast and the tumor are discretized into the Rao, Wilton, Glisson (RWG) triangular patches [46]. The induced equivalent surface currents are approximated, using the vector basis functions, and the integral equations are tested using the same basis functions. A set of linear system of equations is obtained as [25], [47]

$$\begin{pmatrix} \overline{Z}_{S.S} & \overline{Z}_{S.T} \\ \overline{Z}_{T.S} & \overline{Z}_{T.T} \end{pmatrix} \begin{pmatrix} \overline{I}_S \\ \overline{I}_T \end{pmatrix} = \begin{pmatrix} \overline{V}_S \\ 0 \end{pmatrix}. \tag{1}$$

This system of equations incorporates all interactions between elements on the breast and tumor surfaces (i.e., $\overline{Z}_{S.S}$ and $\overline{Z}_{T.T}$, respectively) and elements within the breast and tumor surfaces (i.e., $\overline{Z}_{S.T}$ and $\overline{Z}_{T.S}$). The vector $\overline{V}_S$ represents the tangential components of the incident electric and magnetic fields on the breast surface. This system of equations needs to be solved for the unknown current coefficients $\overline{I}_S$ and $\overline{I}_T$ excited on the breast and tumor surfaces, respectively.

The numerical results in Section III are based on computing the scattered intensity represented by the radar cross section (RCS) defined as [48]

$$\mathrm{RCS} = \frac{4\pi r^2 |\overline{E}^s|^2}{2\eta_0 P^i} \tag{2}$$

where $\overline{E}^s$ is the scattered electric field, P_i is the incident power [49], and r is the distance from the scatterer (i.e., the breast) to the observation point. The RCS will be plotted either versus the frequency or versus the parameter ka, with $k = 2\pi/\lambda_0$, $\lambda_0 = 3 \times 10^8/f$ (m) as the free space wavelength, and f as the frequency of the incident wave. The parameter a represents the radius of the sphere or the larger dimension of the prolate spheroid with $a = 2b$.

Solving (1) using the MoM is computationally very expensive. The MoM, however, will be used for validation. The first method for solving (1) implements the complete SDFMM, which is computationally inefficient when the depth of the tumor is large compared with the free space wavelength. The second method of solving (1) implements the MIM-SDFMM as discussed in [45]. The latter method solves two separate linear systems of equations for the unknown coefficients by exploiting an iterative procedure to update the incident fields on both the breast surface (S) and the tumor surface (T). These two systems of equations are given by [45]

$$\overline{Z}_{S.S}\overline{I}_S^{(n)} = \overline{V}_S^{(n)} \tag{3a}$$

$$\overline{Z}_{T.T}\overline{I}_T^{(n)} = \overline{V}_T^{(n)} \tag{3b}$$

in which $n = 0, 1, 3, \ldots$ represents the number of multiple interactions between the tumor and the breast surface. The value $n = 0$ implies that the induced currents on the breast surface are due to the illuminating source and that no interaction took place with the tumor. The algorithm begins by assuming that no tumors are present in the breast and solving (3a) for the unknown current coefficients on the breast surface, i.e., $\overline{I}_S^{(0)}$. These coefficients are due to the tangential incident fields $\overline{V}_S^{(0)}$. Consequently, the induced electric and magnetic currents on the breast surface, i.e., $\overline{J}_S^{(0)}$ and $\overline{M}_S^{(0)}$ excite the tumor with the fields $\overline{V}_T^{(1)}$ in (3b). These fields are calculated using the near-field surface integrations given by [48]

$$\begin{aligned} \overline{H}_T^A(x,y,z) = &-\frac{1}{4\pi}\int_{S'}\int \left(\hat{R} \times \overline{J}_s(x',y',z')\right) \\ &\times \frac{1+ikR}{R^2}\exp(-ikR)dS' \\ \overline{E}_T^A(x,y,z) = &\frac{1}{i\omega\varepsilon}\nabla \times \overline{H}_T^A \end{aligned} \tag{4a}$$

$$\begin{aligned} \overline{E}_T^F(x,y,z) = &-\frac{1}{4\pi}\nabla \times \int_{S'}\int \overline{M}_s(x',y',z') \\ &\times \frac{\exp(-ikR)}{R}dS' \\ \overline{H}_T^F(x,y,z) = &-\frac{1}{i\omega\mu}\nabla \times \overline{E}_T^F \end{aligned} \tag{4b}$$

where the total electric and magnetic fields are $(\overline{E}^A + \overline{E}^F)$ and $(\overline{H}^A + \overline{H}^F)$, respectively. The superscripts A and F represent fields associated with the vector potentials $\overline{A}$ and $\overline{F}$, respectively. The symbol $\hat{R}$ represents the unit vector between the source and observation points which are separated by the distance R. The wave number of the surrounding medium is given by k with the permittivity and permeability ε and μ, respectively. The differential surface element on the breast is represented by dS'. The next step is to solve (3b) for the unknown coefficients, i.e., $\overline{I}_T^{(1)}$, in order to obtain the electric and magnetic currents on the tumor surface, $\overline{J}_T^{(1)}$ and $\overline{M}_T^{(1)}$, respectively. This process is repeated until the surface current solutions converge.

Using the MIM-SDFMM allows calculating the contribution of each wave interaction between the tumor and the breast interface. This advantage provides insight into the physics involved in the scattering mechanism between the tumor and breast surface. Moreover, it allows the calculation of the induced currents on the breast surface due to only the presence of the tumor [45]. This implies that no subtraction process to obtain the signature of the tumor is used here, leading to faster and more efficient results. In solving (3a), the SDFMM is used to convert the

impedance matrix $\overline{Z}_{S,S}$ to a sparse one. Note that the order of $\overline{Z}_{S,S}$ (associated with the breast) is much larger than the order of the matrix $\overline{Z}_{T,T}$ (associated with the tumor). This is due to the small size of the tumor compared with the breast surface; therefore, it is more efficient to use the SDFMM to solve (3a) and the MoM to solve (3b). The work reported in [45] discusses in detail the computational complexity of the MIM-SDFMM.

The electric and magnetic currents induced on the breast surface due to the tumor alone are $\overline{J}_S = \overline{J}_S^{(1)} + \overline{J}_S^{(2)} + \cdots + \overline{J}_S^{(n)}$, and $\overline{M}_S = \overline{M}_S^{(1)} + \overline{M}_S^{(2)} + \cdots + \overline{M}_S^{(n)}$, respectively. Note that the driving surface currents $\overline{J}_S^{(0)}$ and $\overline{M}_S^{(0)}$ are induced on the breast due to the illuminating source (i.e., transmitting antenna), assuming that no tumors are located inside the breast.

The electromagnetic model discussed above does not incorporate the inhomogeneous breast tissue or the skin thickness (i.e., the skin layer). However, the model incorporates the interface between the air and the breast tissue where the tumor is located. In other words, it accounts for three different homogeneous regions.

It is important to emphasize that the SDFMM is a surface integral equation based algorithm as discussed in [25]–[28] and [43]–[45]. There is no restriction on the shape of the object, assuming that its surface can be disretized into triangular patches. Moreover, the SDFMM does not rely on the symmetry of the object, which is different from the MoM used in [39]. However, the SDFMM cannot simulate a medium if its dielectric constant varies gradually from one point to another. In this case, the volume integral equations could be used instead, where the volume of the scatterer is discretized into volumetric elements. The main advantage of the SDFMM is its $O(N)$ computational complexity for both the CPU time and computer memory, where N is the total number of the surface current unknowns, compared with the MoM which requires $O(N^2)$ to solve the same problem (per iteration).

The electrical properties of breast tissue, the geometry of the breast, the validation with the Mie's solution, the effect of the air-interface, and the computational requirements are key issues. An in depth discussion of these issues follows.

A. Electrical Properties of Breast Tissue

The relative dielectric constants of malignant tumors and normal breast tissue come from measurements reported in the literature [4]–[11]. The frequency dependence of the dielectric constants ($\varepsilon_r = \varepsilon' - j\varepsilon''$) of normal breast tissue and malignant tumors are plotted versus the frequency from 1 to 10 GHz, as shown in Fig. 1. These results are calculated using [20, eq. (1)], which was obtained by curve fitting published measured data up to 3 GHz. Section III will utilize a variety of dielectric constants obtained either from the actual measurement data [4]–[11] or from the curve fitted data of Fig. 1.

B. Breast Geometry

This paper simulates two different geometries of the breast as shown in Fig. 2. In Fig. 2(a), the breast surface is assumed flat, which represents an ideal situation [18]. However, in Fig. 2(b), the breast surface is a 3-D curved geometry, which can represent a patient lying on her back [20], [21]. In the latter case, the geometry is assumed sinusoidal described by $H(x,y) = (h_0/2)(\cos(2\pi\rho/\Lambda) + 1)$; h_0 is the breast height, $\rho = \sqrt{(x-\Lambda/2)^2 + (y-\Lambda/2)^2}$ and $\Lambda = L_x = L_y$ where L_x and L_y are the x and y dimensions, respectively. If the patient is lying on her stomach, the breast will have a more cylindrical shape [22], [23], which will not be considered in Section III.

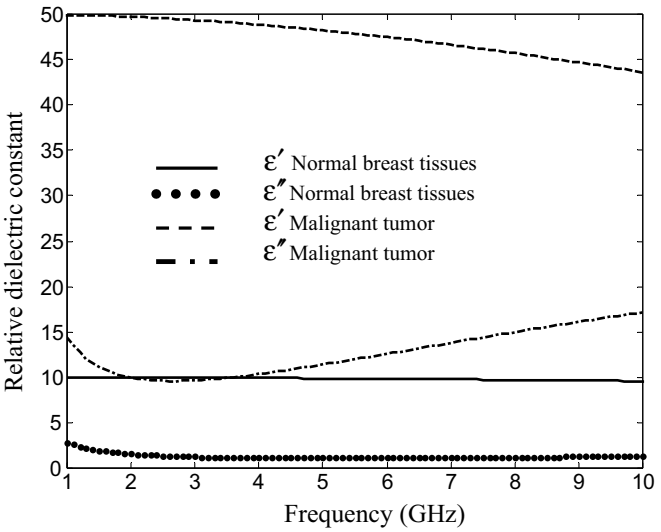

Fig. 1. The relative dielectric constant ($\varepsilon_r = \varepsilon' - j\varepsilon''$) versus frequency for normal and malignant breast tissue obtained from [20].

C. Validation With Mie's Solution [29]

It is important to examine the resonant radiation of a dielectric sphere immersed in air before investigating the more complicated scatterer which contains a sphere immersed in a different medium, as shown in Fig. 2.

The relative dielectric constant $\varepsilon_r = 50 - j12$ simulates the electrical property of a malignant tumor which implies that $\varepsilon_r' = 50$ and the conductivityat $\sigma = \omega\varepsilon''/\varepsilon_0 = 4.0$ S/m at f = 6 GHz [18], [19], [22]. In Example 1, the three dielectric constants of the sphere are: $\varepsilon_r = 50$ (lossless), $\varepsilon_r = 36$ (lossless [29]), and $\varepsilon_r = 50 - j12$ (lossy) as shown in Fig. 3. These results are obtained using the MoM where the sphere is discretized into 764 triangular patches leading to 2292 electric and magnetic unknown coefficients. The plane wave is used for excitation at normal incidence ($\theta' = 0^\circ$) when the electric field is polarized in the x-direction as shown in Fig. 3. The electric field in this case is parallel to the plane of incidence ($z - x$ plane), which represents the vertical polarization (V-pol.). All results of Fig. 3 are for the copolarized scattered waves in the backscatter direction. The results show that the RCS of lossless spheres exhibits sharp resonant scattering upon varying the parameter ka. The results of the lossless sphere with $\varepsilon_r = 36$ show full agreement with those obtained using the Mie solution reported in [29]. Note that the magnitude of the RCS is greatly reduced when the sphere becomes lossy ($\varepsilon_r = 50 - j12$). Moreover, the sharp peaks are not shown for the lossy sphere (see Fig. 3).

D. Effect of the Air-Interface

Example 2 investigates the effect of the presence of the air-interface on the observed resonance scattering. A lossless sphere

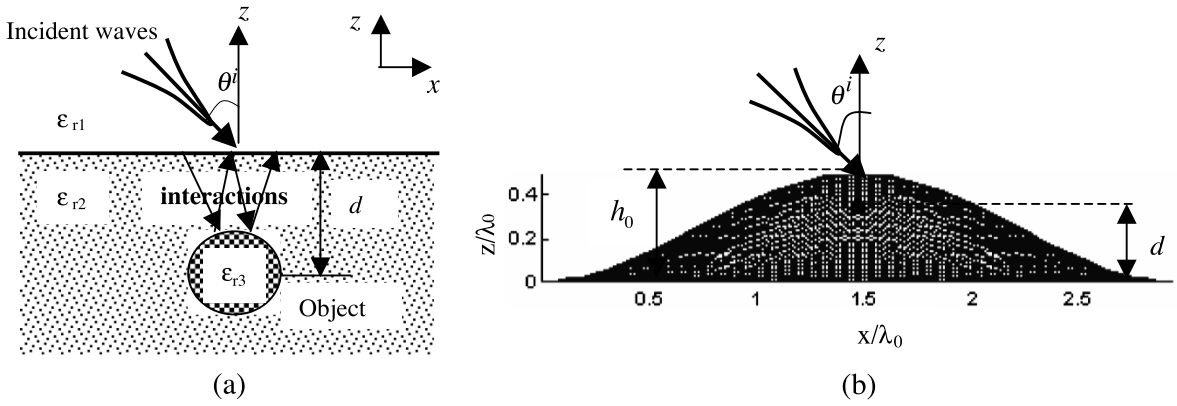

Fig. 2. Cross section of a spherical tumor located beneath (a) a flat air-breast interface showing multiple interactions with $n = 2$. (b) Side view of the 3-D curved breast geometry.

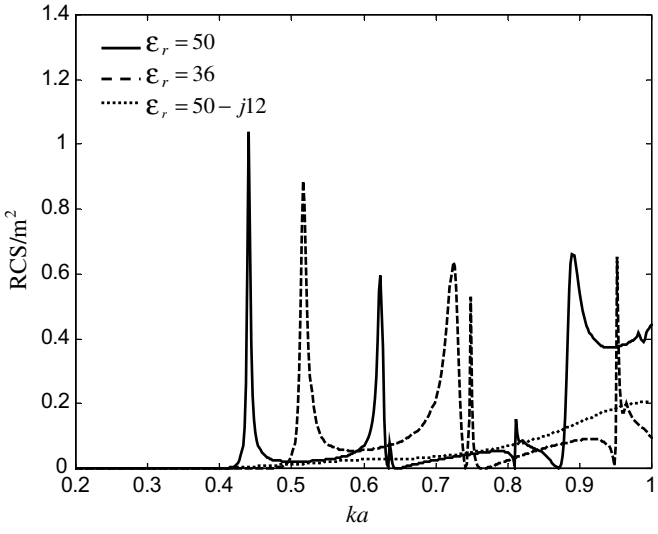

Fig. 3. Copolarized backscatter RCS versus the normalized radius ka of a sphere immersed in air for three cases with relative dielectric constants as $\varepsilon_r = 50 - j12$, 50, and 36. Normal incidence and V-polarization.

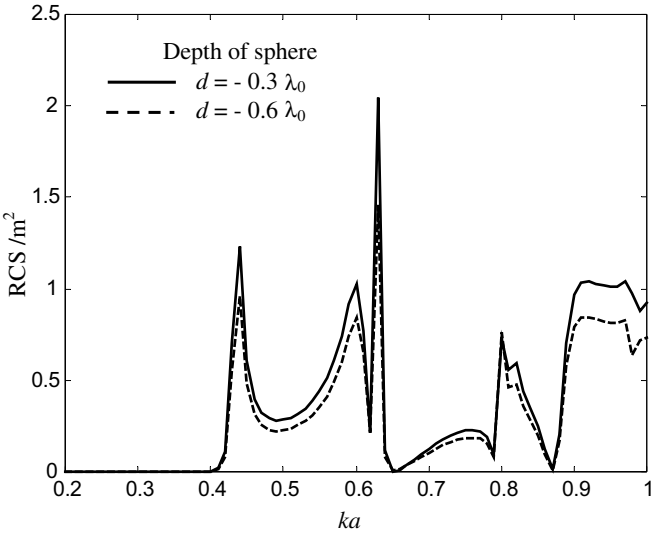

Fig. 4. Copolarized backscatter RCS versus the normalized radius ka of the sphere only. The flat interface depicted in Fig. 2(a) is used with $\varepsilon_{r1} = 1$ (air), $\varepsilon_{r2} = 2.0 - j0.1$, and $\varepsilon_{r3} = 50$ at two depths ($d = -0.3\lambda_0$ and $-0.6\lambda_0$). Normal incidence and H-polarization.

with $\varepsilon_{r3} = 50$ is located beneath the flat interface of Fig. 2(a) at depth d, measured from its center. The surrounding medium is slightly lossy with $\varepsilon_{r2} = 2 - j0.1$. To eliminate the edge excitations, the interface is illuminated using plane waves tapered toward the edges of the flat surface, i.e., using a Gaussian beam as discussed in [25] and [50]. The incident waves are in the normal direction with the electric field polarized in the y-direction, i.e., perpendicular to the plane of incidence ($z-x$ plane), which represents the horizontal polarization (H-pol.). The RCS for only the immersed sphere is plotted versus ka in the backscatter direction as shown in Fig. 4.

The dimensions of the modeled flat surface (i.e $L_x \times L_y$) are $2.94\lambda_0 \times 2.94\lambda_0$ and the sphere is located beneath the surface at depths $d = -0.3\lambda_0$ and $d = -0.6\lambda_0$, respectively, as shown in Fig. 4. This paper utilizes the incident Gaussian beam with a width equal to $1.2\lambda_0$. The flat interface is discretized into 4802 triangular patches (i.e., the discretization rate is $0.06\lambda_0$) leading to 14 210 electric and magnetic unknown coefficients. For each depth value d, the MIM-SDFMM computer code was run 81 times for ka values ranging from 0.2 to 1 with a step equal to 0.01.

In Fig. 4, the RCS results clearly exhibit sharp peaks at certain values of the parameter ka despite the presence of the air-interface. It is important to mention that finer resolution of ka could lead to increasing the magnitude of the peaks. The results indicate that the magnitude of the sharp peaks decreases when the depth increases, as shown in Fig. 4.

E. Computational Issues

It is important to emphasize that varying the parameter ka in each run requires solving both (2a) and (2b) once except when the computer code begins; then solving (2a) twice is required. This saves more than 30% of the computation time. The total CPU required to obtain these solutions is approximately 22 h for a full curve in Fig. 4 (i.e., for 81 runs). The computations were conducted on the Compaq Alpha Server (GS140 EV6) with 667-MHz clock speed. Moreover, to speed up the computations, only a single interaction between the object and the interface is considered (i.e., $n = 1$), as discussed earlier. Insignificant differences were observed when higher order interactions were considered (i.e., for $n = 2, 3, \ldots$). The same observation

was reported in [45], particularly when the surrounding medium was lossy. This justifies accounting only for the first interaction (i.e., $n = 1$) in all numerical results presented in Section III.

III. Numerical Results

This section presents several examples of the resonance spectra of malignant tumors located in normal breast tissue. Examples 3–9 investigate the effect of the shape, depth, electrical properties, and orientation of the tumor. Moreover, this paper looks into the effect of changing the electrical properties of normal breast tissue, breast geometry, polarization, and the direction and frequency of the incident electromagnetic waves. The discussion is as follows:

A. Depth of the Tumor

In Example 3, a lossy medium is assumed in order to simulate normal breast tissue properties at microwave frequencies. The dielectric constant is assumed $\varepsilon_{r2} = 9.0 - j1.2$ which implies that $\varepsilon_r' = 9.0$ and $\sigma = 0.4$ S/m at f $= 6$ GHz [18], [19], [22]. The lossy sphere of dielectric constant $\varepsilon_{r3} = 50 - j12$ to simulate the malignant tumor, is located under the flat interface of Fig. 2(a) at a variety of depths from $d = -0.3\lambda_0$ to $d = -0.7\lambda_0$, as shown in Fig. 5(a). The copolarized backscattered RCS of the tumor alone clearly exhibits a resonance scattering behavior even when it is located in a lossy medium. These results show that the resonance phenomenon of the tumor survived the presence of the interface and the lossy surrounding environment. However, the depth of the tumor affected the magnitude of the spectra, but not the resonance locations.

B. Electrical Properties

It is also important to investigate a variety of electrical properties of breast tissue and tumor on resonant scattering, as shown in Fig. 5(b). The dielectric values are obtained from the measurements reported in the literature as: 1) $\varepsilon_{r2} = 9.0 - j1.2$, $\varepsilon_{r3} = 50.0 - j12$ at f $= 6$ GHz [18], [19], [22]; 2) $\varepsilon_{r2} = 10 - j1.97$, $\varepsilon_{r3} = 45 - j16.87$ at f $= 3.2$ GHz (the lower limit values reported in [8, Table 5]); 3) $\varepsilon_{r2} = 9.8 - j2.08$, $\varepsilon_{r3} = 46 - j25.87$ at f $= 3.2$ GHz (for patient no. 37 reported in [8, Table 2]); 4) $\varepsilon_{r2} = 15 - j3.6$, $\varepsilon_{r3} = 52 - j18.4$ at f $= 1$ GHz reported in [10]; and 5) $\varepsilon_{r2} = 25 - j5.9$, $\varepsilon_{r3} = 60 - j22.49$ at f $= 3.2$ GHz (the upper limit values reported in [8, Table 5]). As expected, when the normal breast tissue became more lossy, the scattering magnitude at resonant frequencies (i.e., the maximum points) decreased, as shown in Fig. 5(b).

C. Multiple Frequencies

Example 4 investigates resonant scattering versus the frequency from 1 to 10 GHz. This example utilizes the dielectric constants presented in Fig. 1 [20]. Note that the real and imaginary parts of the dielectric constants of normal breast tissue are almost constant in this range of frequency, which is not the case for a malignant tumor. To speed-up the calculations, only the change in the dielectric constant of malignant tumor is incorporated in the computer code, keeping the dielectric constant of normal tissue at $\varepsilon_r = 10 - j1.2$ (see Fig. 1). This approximation justifies computing and storing the impedance matrix associated with the breast ($\overline{Z}_{S,S}$) only once, when the computer code begins, leading to a substantial saving in computation time. In Fig. 6, the backscatter RCS at normal incidence is plotted versus the frequency from 1 to 10 GHz in steps of 100 MHz. The tumor is modeled as a sphere of radius a ranging from 1 to 6 mm, and is located beneath the flat surface of Fig. 2(a) at $d = -1$ cm and $d = -5$ cm, as shown in Fig. 6, respectively. As expected, the results show that the spectrum of the tumor varies with the radius a; however, when the radius becomes 2 mm or less, a larger frequency range will be needed. This indicates the difficulty in detecting small tumors (less than 2 mm), since the surrounding medium becomes more lossy at higher frequencies. Moreover, upon comparing the results of Fig. 6(a) with those of 6(b), it is clear that the depth of the tumor affects the magnitude of the spectra rather than their locations.

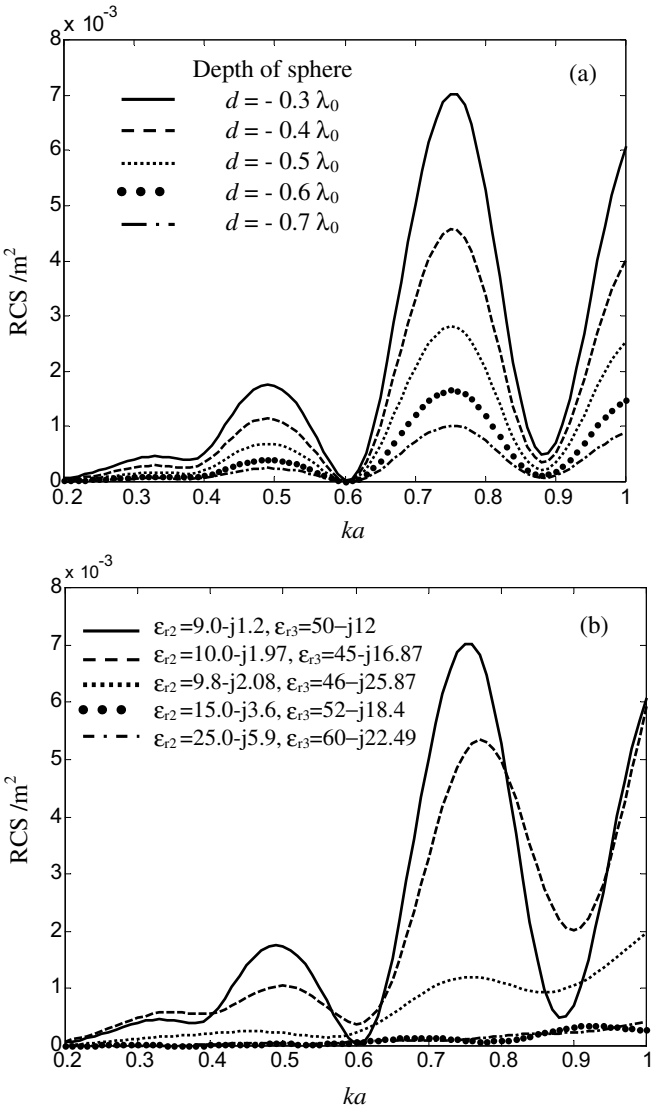

Fig. 5. Copolarized backscatter RCS versus the normalized radius ka of the spherical tumor only for: (a) $\varepsilon_{r2} = 9.0 - j1.2$ and $\varepsilon_{r3} = 50 - j12$ for breast and tumor tissue, respectively, (b) with a variety of dielectric constants for breast and tumor tissue. Normal incidence and H-polarization.

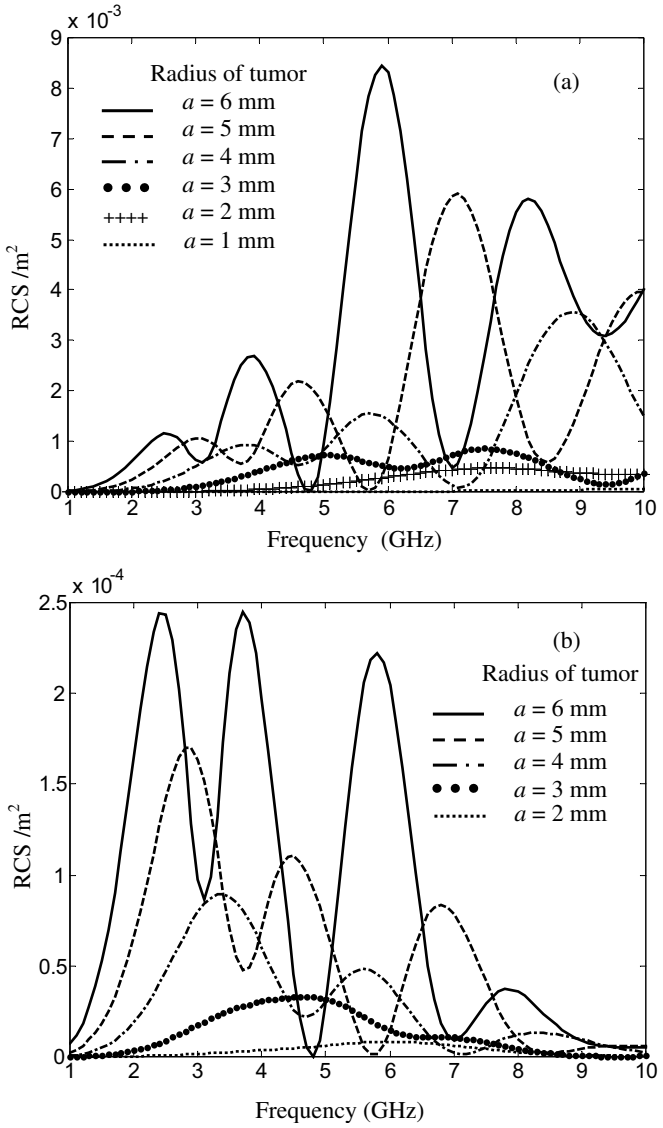

Fig. 6. Copolarized backscatter RCS versus the frequency for the spherical malignant tumor only with dielectric constants varying with frequency (see Fig. 1). Normal breast tissue has $\varepsilon_{r2} = 10.0 - j\,1.2$, when the breast is flat as depicted in Fig. 2(a) at depth (a) $d = 1$ cm, (b) $d = 5$ cm. Normal incidence and H-polarization.

D. Incident and Scatter Directions and Polarizations

Example 5 investigates a variety of incident directions. The 3-D curved geometry depicted in Fig. 2(b) is used in this example. In Fig. 7(a)–(c), the RCS of the spherical tumor only is plotted as function of the parameter ka. In this example, the depth of the tumor is $d = +0.3\lambda_0$, and the breast height is $h_0 = 0.5\lambda_0$ [see Fig. 2(b)]. The copolarized RCS for the H-polarization at normal incidence ($\vartheta^i = 0^\circ$) are shown in Fig. 7(a). The scattered waves are received in three directions: 1) $\vartheta^s = 0^\circ$ (backscatter direction); 2) $\vartheta^s = 45^\circ$, $\phi^s = 0$ (forward direction); and 3) $\vartheta^s = 45^\circ$, $\phi^s = \pi^\circ$ (backward direction). The dielectric constants are assumed as $\varepsilon_{r2} = 9.0 - j1.2$ and $\varepsilon_{r3} = 50.0 - j12$ for the normal breast tissue and the malignant tumor, respectively. As expected, the scattered intensity in the backscatter direction at normal incidence is larger than that in the forward or in the backward directions, as shown in Fig. 7(a).

In Fig. 7(b)-(c), the copolarized scattered RCS at the oblique incident direction $\vartheta^i = 45^\circ$, $\phi^i = 0^\circ$, are plotted for the H- and V-polarizations, respectively. The results clearly show the resonant scattering for both polarizations at all three scattering directions ($\vartheta^s = 0^\circ$, $\vartheta^s = 45^\circ$, $\phi^s = 0^\circ$, and $\vartheta^s = 45^\circ$, $\phi^s = \pi$). Larger magnitudes were observed in the V-polarization case shown in Fig. 7(c). For the H-polarization, the magnitude at resonant frequencies (i.e., the maximum points) occurs almost at the same locations for all three scattering directions, as shown in Fig. 7(b). However, for the V-polarization case, some of these locations are shifted upon changing the scattering direction as shown in Fig. 7(c). Interestingly, only in the backscatter direction (i.e.,$\vartheta^s = 45^\circ$, $\phi^s = \pi$), the maximum points occur at the same locations for both the H- and V-polarization, as shown in Fig. 7(b)-(c), respectively.

It is important to mention that the forward direction defined in this paper indicates scattering in all directions above the air-interface, where the receiving antenna is located (i.e., above the breast surface). This definition is completely different from the forward direction for scattering from a sphere immersed in free space, which is exactly 180° from the incident direction as described by Larsen *et al.* [3]. No resonance was observed in the forward direction in the results presented by Larsen *et al.* [3], which is not the case in the current work, as clearly demonstrated in Fig. 7(a)–(c).

E. Total Scattered Intensity and Validation With the MoM

As discussed in Section II, the above resonance scattering is obtained by calculating the electric and magnetic surface currents induced on the breast surface due to the presence of the malignant tumor. However, the currents induced on the breast surface due to the incident waves (i.e., from the transmitting antenna) cannot be differentiated from those induced due to the wave interactions with the tumor. In other words, the surface current induced on the breast is the summation in complex vectors of both currents as discussed in Section II.

Therefore, in Example 6, the total currents induced on the breast surface are used to obtain the total scattering intensity. These results are for the H-polarization at normal incidence with the same dielectric constants and depth of Fig. 7. The results clearly exhibit the resonance phenomenon compared with the case where no tumor was present. In order to validate these results, a second multiple interaction between the tumor and the breast surface (i.e., $n = 2$) is taken into account, showing full agreement with those produced using $n = 1$. In addition, the MoM is used to validate both cases demonstrating good agreement, with acceptable errors for larger ka. Note that Fig. 8 shows the maximum magnitude of the resonance as 0.35, while Fig. 7(a) shows a maximum magnitude of 0.015. This drop in the magnitude is due to using the same incident power (P^i) to normalize the RCS results in both cases.

F. Nonspherical Tumor

Example 7 investigates nonspherical malignant tumors. The tumor is assumed to have a prolate spheroid shape. The curved breast geometry depicted in Fig. 2(b) is used here. The dimensions of the prolate spheroid are given by a and b with $a = 2b$.

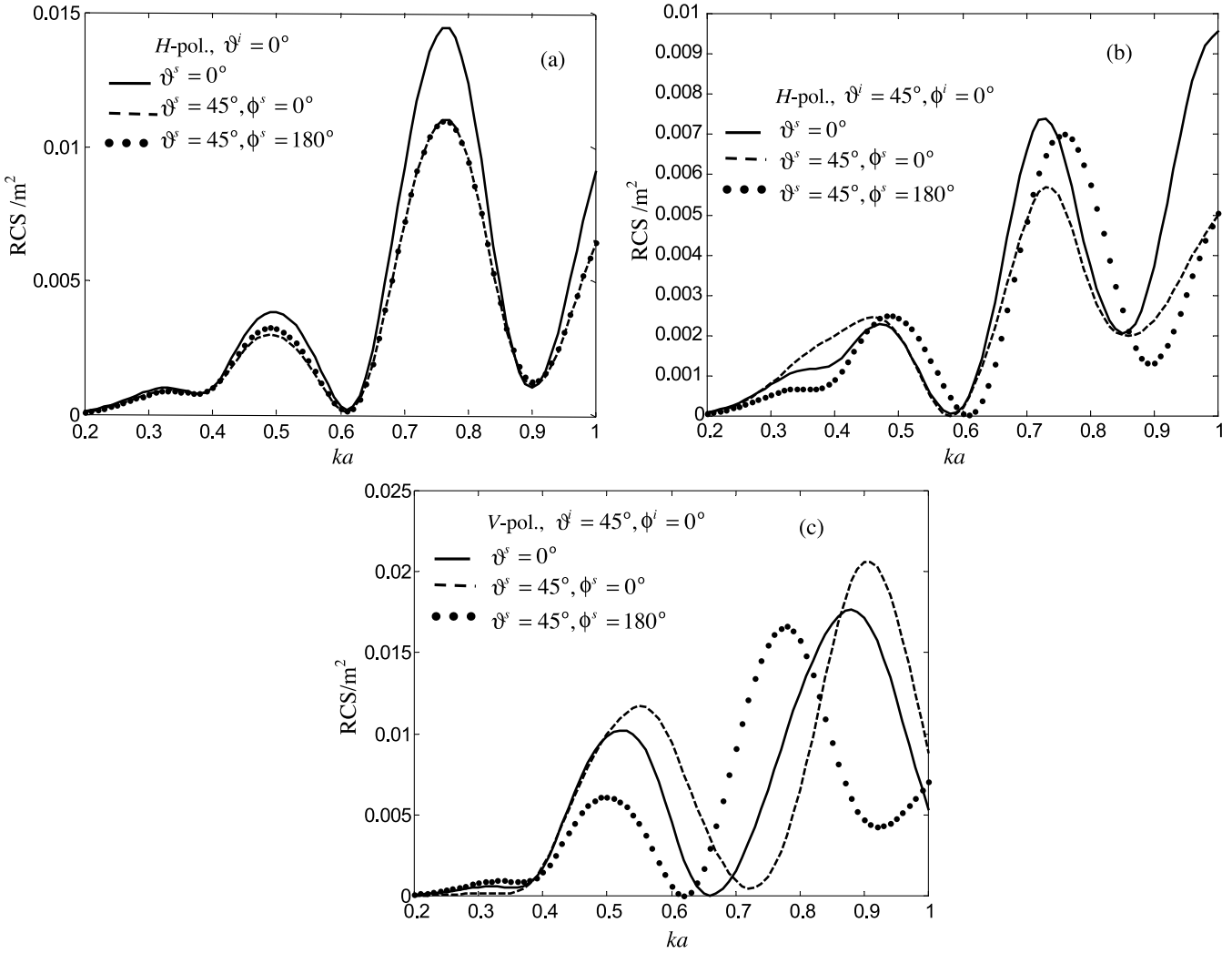

Fig. 7. Copolarized RCS versus the normalized radius ka of the spherical malignant tumor only with $\varepsilon_{r3} = 50 - j12$. It is located at $d = +0.3\lambda_0$ in normal breast tissue ($\varepsilon_{r2} = 9.0 - j1.2$) as depicted in Fig. 2(b) for (a) $\vartheta^i = 0°$ H-polarization, (b) $\vartheta^i = 45°$, H-polarization, and (c) $\vartheta^i = 45°$, V-polarization.

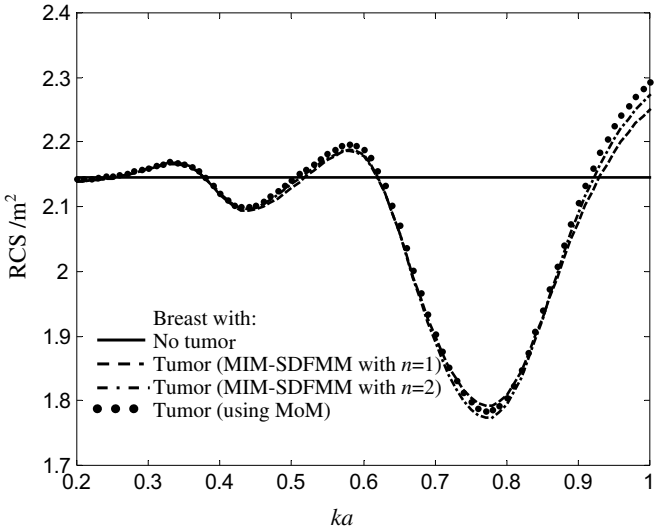

Fig. 8. Copolarized backscatter RCS versus the normalized radius ka of the spherical malignant tumor with $\varepsilon_{r3} = 50 - j12$, at $d = +0.3\lambda_0$ in normal breast tissue with $\varepsilon_{r2} = 9.0 - j1.2$ [see Fig. 2(b)]. Normal incidence and H-polarization. These results are for the whole scatterer (i.e., the breast with the tumor).

Three incident directions are used: 1) $\theta^i = 0°$; 2) $\theta^i = 45°$, $\phi^i = 0$; and 3) $\theta^i = 25°$, $\phi^i = 130°$ for both the H- and V-polarizations. The dielectric constants are assumed as $\varepsilon_{r2} = 9.0 - j1.2$ for the normal breast tissue and $\varepsilon_{r3} = 50.0 - j12$

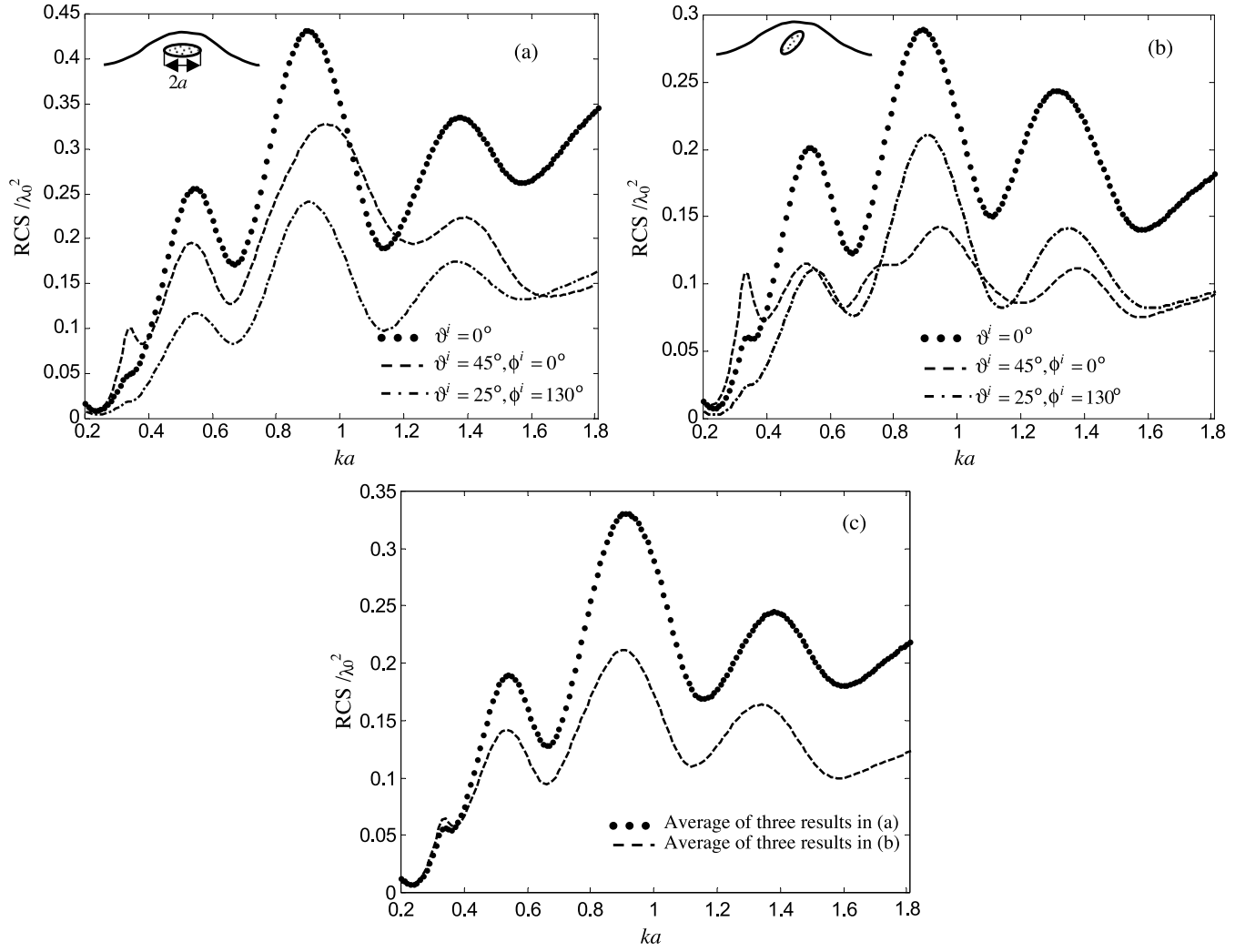

Fig. 9. Normalized average RCS versus the normalized radius ka of the prolate spheroid tumor only ($\varepsilon_{r3} = 50 - j12$), in normal breast tissue ($\varepsilon_{r2} = 9.0 - j1.2$), where $a = 2b$ for: (a) horizontally oriented prolate spheroid at depth $d = +0.3\lambda_0$, (b) randomly oriented prolate spheroid at depth $d = +0.25\lambda_0$, and (c) the average of (a) and (b) with respect to the three incident directions.

for the malignant tumor. In this example, the original definition of the RCS of (2) is used, but integrates the scattered intensity over the scattering directions in the plane of incidence, i.e., $\theta^s = 0°, 1°, 2° \cdots, 89°$ at both $\phi^s - \phi^i = 0°$ (forward direction) and $\phi^s - \phi^i = 180°$ (backward direction). The RCS is normalized by the cross section area πa^2.

In this example, the average RCS with respect to polarization (i.e., the H- and V-polarization) is plotted versus ka, as shown in Fig.9 (a)–(c). In Fig. 9(a), the results are shown for the malignant tumor only, which is horizontally oriented at depth $d = +0.3\lambda_0$ measured from its center. In this case, the Euler's angles are $\alpha_x = \beta_y = \gamma_z = 0°$. On the other hand, in Fig. 9(b), the results are shown for the same tumor, but when it is randomly oriented at $d = +0.25\lambda_0$. In this case, the Euler's angles are $\alpha_x = 10°$, $\beta_y = 15°$, and $\gamma_z = 5°$. Interestingly, the results of Fig. 9(a)–(b) shows that the resonance occurs almost at the same values of ka regardless of the incident direction. However, comparing Fig.9 (a)–(b) shows that the magnitude of the resonance spectra depends on both the incident angle and the orientation of the tumor.

G. Averaging

The results in Fig. 9(a)–(b) suggest that taking the average with respect to the incident directions can produce invariant spectra of the malignant tumor regardless of its orientation, as shown in Fig. 9(c). Notice that the two spectra shown in Fig. 9(c) look very similar, except for the magnitude, which is due to the difference in the depth [$0.3\lambda_0$ in Fig. 9(a) versus $0.25\lambda_0$ in Fig. 9(b)]. These results indicate that the spectra of the malignant tumor are invariant with the incident polarization and the incident and scattered directions. However, these spectra depend on the physical characteristics of the tumor, i.e., the shape and the electrical properties of its tissue. These conclusions agree with the results reported in [29] in which lossless objects were immersed in free space. Moreover, the results show that the depth affects the scattering magnitude rather than the resonance locations, as shown in Fig. 9(c). This observation also agrees with the results reported in [39], where the natural resonant frequencies of a mine, buried in dispersive layered half space, were investigated versus its burial depth. Interestingly, the spectra of the spherical tumor shown in Fig. 7 are different from those of

the spheroid tumors shown in Fig. 9, which agrees with the conclusions reported in [29]. This observation can be explored to distinguish malignant from benign tumors, as mentioned in [18].

In this paper, the malignant tumor was modeled by symmetric, smooth and compact objects such as spheres and prolate spheroids. However, in reality, malignant tumors tend to have irregular shapes. It is not possible to discretize these irregular surfaces into the triangular patches needed for the MoM without using a sophisticated discretization software, which is not available at this point. It is necessary to resolve this issue before using the presented approach to discriminate between malignant and benign breast tumors, because their resonance spectra are expected to be substantially different.

The current paper can be a guide in the selection of the frequency range at which the tumor resonates, providing a maximum signature at the receiver. It is essential to also investigate the effect of the skin thickness and breast inhomogeneities on the resonance phenomenon. The skin layer is a strong scatterer at the frequency range 1–10 GHz, therefore, it is important to include it in the model. This issue will be investigated in a future work.

IV. Conclusion

This paper utilized the fast algorithm, MIM-SDFMM to investigate the resonance scattering of malignant breast cancer tumors. The results indicate that the resonance scattering phenomenon is invariant with the incident polarization, the incident or scattered directions, and the depth of the tumor. The spectra vary only with the shape and material of the tumor. This indicates the resonance spectra to be a unique characteristic of the tumor which can be explored to detect and discriminate between malignant and benign breast tumors, as they differ drastically in shape and material.

Acknowledgment

The author would like to thank W. Lawrence, J. Johnson, M. Deshpande, and W. Munden at NASA for their valuable comments and discussions.

References

[1] M.Manfred Säbel and H.Horst Aichinger, "Recent developments in breast imaging," *Phys. Med. Bio.*, vol. 41, pp. 315–368, 1996.

[2] K. Großhadern, "Nonmammographic breast imaging techniques," *Curr. Opinion Radiol.*, no. 4, pp. 146–154, 1992.

[3] L. E. Larsen and J. H. Jacobi, "Methods of microwave imagery," in *Medical Applications of Microwave Imaging*. Piscataway, NJ: IEEE Press, 1986, pp. 118–137.

[4] C. Gabriel, S. Gabriel, and E. Corthout, "The dielectric properties of biological tissues: I. Literature survey," *Phys. Med. Biol.*, vol. 41, pp. 2231–2249, 1996.

[5] S. Gabriel, R. W. Lau, and C. Gabriel, "The dielectric properties of biological tissues: II. Measurements in the frequency range 10 Hz to 20 GHz," *Phys. Med. Biol.*, vol. 41, pp. 2251–2269, 1996.

[6] ——, "The dielectric properties of biological tissues: III. Parametric models for dielectric spectrum of tissues," *Phys. Med. Biol.*, vol. 41, pp. 2271–2293, 1996.

[7] T. Joines, Y. Z. C. Li, and R. L. Jirtle, "The measured electrical properties of normal and malignant human tissues from 50 to 900 MHz," *Med. Phys.*, vol. 21, no. 4, pp. 547–550, Apr. 1994.

[8] A. M. Campbell and D. V. Land, "Dielectric properties of female human breast tissue measures *in vitro* at 3.2 GHz," *Phys. Med. Biol.*, vol. 37, no. 1, pp. 193–210, 1992.

[9] A. J. Surowiec, S. S. Stuchly, J. R. Barr, and A. Swarup, "Dielectric properties of breast carcinoma and the surrounding tissues," *IEEE Trans. Biomed. Eng.*, vol. 35, pp. 257–263, Apr. 1988.

[10] S. Chaudhary, R. K. Mishra, A. Swarup, and J. M. Thomas, "Dielectric properties of normal and malignant human breast tissues at radioactive and microwave frequencies," *Ind. J. Biochem. Biophys.*, vol. 21, pp. 76–79, Feb. 1984.

[11] R. Peloso, D. T. Tuma, and R. K. Jain, "Dielectric properties of solid tumors during normothermia and hyperthermia," *IEEE Trans. Biomed. Eng.*, vol. BME-31, pp. 725–728, Nov. 1984.

[12] A. E. Souvorov, A. E. Bulyshev, S. Y. Semenov, R. H. Svenson, and G. P. Tatsis, "Two-dimensional computer analysis of a microwave flat antenna array for breast cancer tomography," *IEEE Trans. Microwave Theory Tech.*, vol. 48, pp. 1413–1415, Aug. 2000.

[13] A. E. Bulyshev, A. E. Souvorov, S. Y. Semenov, R. H. Svenson, A. G. Nazarov, Y. E. Sizov, and G. P. Tatsis, "Three-dimensional microwave tomography: theory and computer experiments in scalar approximation," *Inverse Problems*, vol. 16, pp. 863–875, 2000.

[14] P. M. Meaney, M. W. Fanning, D. Li, S. P. Poplack, and K. D. Paulsen, "A clinical prototype for active microwave imaging of the breast," *IEEE Trans. Microwave Theory Tech.*, vol. 11, pp. 1841–1853, 2000.

[15] P. M. Meaney, K. D. Paulsen, J. T. Chang, M. W. Fanning, and A. Hartov, "Nonactive antenna compensation for fixed-array microwave imaging: part I. Model development," *IEEE Trans. Med. Imag.*, vol. 18, pp. 508–518, June 1999.

[16] ——, "Nonactive antenna compensation for fixed-array microwave imaging: part II. Imaging results," *IEEE Trans. Med. Imag.*, vol. 18, pp. 508–518, June 1999.

[17] P. M. Meaney, K. D. Paulsen, and J. T. Chang, "Near-field microwave imaging of biologically-based materials using a monopole transceiver system," *IEEE Trans. Microwave Theory Tech.*, vol. 46, pp. 31–45, 1998.

[18] S. Hagness, A. Taflove, and J. E. Bridges, "Three-dimensional FDTD analysis of a pulsed microwave confocal systems for breast cancer detection: design of an antenna-array element," *IEEE Trans. Antennas Propagat.*, vol. 47, pp. 783–791, May 1999.

[19] S. C. Hagness, A. Taflove, and J. E. Bridges, "Two-dimensional FDTD analysis of a pulsed microwave confocal system for breast cancer detection: fixed-focus and antenna-array sensors," *IEEE Trans. Biomed. Eng.*, vol. 45, pp. 1470–1479, Dec. 1998.

[20] X. Li and S. C. Hagness, "A confocal microwave imaging algorithm for breast cancer detection," *IEEE Microwave Wireless Components Lett.*, vol. 11, pp. 130–132, Mar. 2001.

[21] E. J. Bond, X. Li, S. Hagness, and B. D. Van Veen, "Microwave imaging via space-time beamforming for early detection of breast cancer," in *Proc. IEEE Int. Conf. Acoustics, Speech, and Signal Processing*, vol. 3, May 13–17, 2000, pp. 2909–2912.

[22] E. C. Fear and M. A. Stuchly, "Microwave detection of breast cancer," *IEEE Trans. Microwave Theory Tech.*, vol. 46, pp. 1854–1863, Nov. 2000.

[23] ——, "Microwave system for breast tumor detection," *IEEE Trans. Microwave Theory Tech.*, vol. 9, pp. 470–472, Nov. 1999.

[24] E. C. Fear, S. C. Hagness, P. M. Meaney, M. Okoniewski, and M. Stuchly, "Enhancing breast tumor detection with near-field imaging," *IEEE Microwave Mag.*, pp. 48–56, Mar. 2002.

[25] M. El-Shenawee, C. Rappaport, E. Miller, and M. Silevitch, "3-D subsurface analysis of electromagnetic scattering from penetrable/PEC objects buried under rough surfaces: use of the steepest descent fast multipole method (SDFMM)," *IEEE Trans. Geosci. Remote Sensing*, vol. 39, pp. 1174–1182, June 2001.

[26] M. El-Shenawee, C. Rappaport, and M. Silevitch, "Monte Carlo simulations of electromagnetic wave scattering from random rough surface with 3-D penetrable buried object: mine detection application using the SDFMM," *J. Opt. Soc. Amer. A*, vol. 18, no. 12, pp. 3077–3084, Dec. 2001.

[27] M. El-Shenawee, "Scattering from multiple objects buried under two-dimensional randomly rough surface using the steepest descent fast multipole method," *IEEE Trans. Antennas Propagat.*, vol. 51, pp. 802–809, Apr. 2003.

[28] M. El-Shenawee and C. Rappaport, "Monte Carlo simulations for the statistics of clutter in minefields: AP mine-like target buried near a dielectric object beneath two-dimensional randomly rough ground," *IEEE Trans. Geosci. Remote Sensing*, vol. 40, June 2002.

[29] P. W. Barber, J. F. Owen, and R. K. Chang, "Resonant scattering for characterization of axisymmetric dielectric objects," *IEEE Trans. Antennas Propagat.*, vol. AP-30, pp. 168–172, Mar. 1982.

[30] B. L. Merchant, P. J. Moser, A. Nagl, and H. Uberall, "Complex pole patterns of the scattering amplitude for conducting spheroids and finite-length cylinders," *IEEE Trans. Antennas Propagat.*, vol. 36, pp. 1769–1777, Dec. 1988.

[31] A. W. Glisson, D. Kajfez, and J. James, "Evaluation of modes in dielectric resonators using a surface integral equation formulation," *IEEE Trans. Microwave Theory Tech.*, vol. MTT-31, pp. 1023–1029, Dec. 1983.
[32] D. Kajfez, A. W. Glisson, and J. James, "Computed modal field distribution for isolated dielectric resonators," *IEEE Trans. Microwave Theory Tech.*, vol. MTT-32, pp. 1609–1616, Dec. 1984.
[33] J. V. Bladel, "On the resonances of a dielectric resonators of very high permittivity," *IEEE Trans. Microwave Theory Tech.*, vol. MTT-23, pp. 199–208, Feb. 1975.
[34] P. Affolter and B. Eliasson, "Electromagnetic resonances and Q-factors of lossy dielectric spheres," *IEEE Trans. Microwave Theory Tech.*, vol. MTT-21, pp. 573–578, Sept. 1973.
[35] M. Gastine, L. Courtois, and J. L. Dormann, "Electromagnetic resonancse of free dielectric spheres," *IEEE Trans. Microwave Theory Tech.*, vol. MTT-15, pp. 694–700, Dec. 1967.
[36] J. V. Bladel, "The excitation of dielectric resonators of very high permittivity," *IEEE Trans. Microwave Theory Tech.*, vol. MTT-23, pp. 208–217, Feb. 1974.
[37] D. J. Burr and Y. T. Lo, "Remote sensing of complex permittivity by multipole resonances in RCS," *IEEE Trans. Antennas Propagat.*, vol. AP-21, pp. 554–561, July 1973.
[38] S. Lin and G. W. Hanson, "An efficient full-wave method for analysis of dielectric resonators possessing separable geometries immersed in inhomogeneous environment," *IEEE Trans. Microwave Theory Tech.*, vol. 48, Jan. 2000.
[39] N. Geng, D. R. Jackson, and L. Carin, "On the resonances of a dielectric BOR buried in a dispersive layered medium," *IEEE Trans. Antennas Propagat.*, vol. 47, pp. 1305–1313, Aug. 1999.
[40] J. R. Arias-Gonzalez, M. Nieto-Vesperinas, and A. Madrazo, "Morphology-dependent resonances in the scattering of electromagnetic waves from an object buried beneath a plane or a random rough surface," *J. Opt. Soc. Amer., A*, vol. 16, no. 12, pp. 2928–2934, Dec. 1999.
[41] V. Rokhlin, "Rapid solution of integral equations of scattering theory in two dimensions," *J. Comput. Phys.*, vol. 36, pp. 414–439, 1990.
[42] C. C. Lu and W. C. Chew, "A multilevel fast-algorithm for solving a boundary integral equation of wave scattering," *Microwave Opt. Tech. Lett.*, vol. 7, pp. 466–470, July 1994.
[43] V. Jandhyala, "Fast multilevel algorithms for the efficient electromagnetic analysis of quasi-planar structures," Ph.D. dissertation, Dept. Elect. Comput. Eng., Univ. Illinois at Urbana-Champaign, 1998.
[44] M. El-Shenawee, V. Jandhyala, E. Michielssen, and W. C. Chew, "The steepest descent fast multipole method (SDFMM) for solving combined field integral equation pertinent to rough surface scattering," in *Proc. IEEE APS/URSI '99 Conf.*, Orlando, FL, July 1999, pp. 534–537.
[45] M. El-Shenawee, "The multiple interaction model for nonshallow scatterers buried beneath two-dimensional random rough surfaces," *IEEE Trans. Geosci. Remote Sensing*, vol. 40, pp. 982–987, Apr. 2002.
[46] S. M. Rao, D. R. Wilton, and A. W. Glisson, "Electromagnetic scattering by surfaces of arbitrary shape," *IEEE Trans. Antennas Propagat.*, vol. AP-30, pp. 409–418, May 1982.
[47] L. Medgyesi-Mitschang, J. Putnam, and M. Gedera, "Generalized method of moments for three-dimensional penetrable scatterers," *J. Opt. Soc. Amer., A*, vol. 11, no. 4, pp. 1383–1398, Apr. 1994.
[48] C. A. Balanis, *Advanced Engineering Electromagnetics*: John Wiley & Sons Inc., 1989, ch. 6, pp. 254–309.
[49] R. L. Wagner, J. Song, and W. C. Chew, "Monte Carlo simulation of electromagnetic scattering from two-dimensional random rough surfaces," *IEEE Trans. Antennas Propagat.*, vol. 45, pp. 235–245, Feb. 1997.
[50] P. Tran and A. A. Maradudin, "Scattering of a scalar beam from a two-dimensional randomly rough hard wall: enhanced backscatter," *Phy. Rev. B*, vol. 45, no. 7, pp. 3936–3939, Feb. 1992.

Magda El-Shenawee (S'90–M'91–SM'02) received the B.S. and M.S. degrees in electrical engineering from Assiut University, Assiut, Egypt, and the Ph.D. degree in electrical engineering from the University of Nebraska-Lincoln in 1991.

In 1992, she worked as a Research Associate in the Center for Electro-Optics at the University of Nebraska where she focused on the problem of enhanced backscatter phenomena. In 1994, she worked as a Research Associate at the National Research Center, Cairo, Egypt, and in 1997, she worked as Visiting Scholar at the University of Illinois at Urbana-Champaign. In 1999, she joined the Multidisciplinary University Research Initiative (MURI) team at Northeastern University, Boston, MA. Currently, she is an Assistant Professor with the Department of Electrical Engineering at the University of Arkansas, Fayetteville. Her research areas are rough surface scattering, computational electromagnetics, subsurface sensing of buried objects, breast cancer modeling, computational imaging, numerical methods, and micro-strip circuits.

Dr. El-Shenawee is a member of Eta Kappa Nu electrical engineering honor society.